Journal of Physics D: Applied Physics

PAPER

Operation-mode recognition of surface microdischarge based on visible image and deep learning

To cite this article: Chen Lu *et al* 2022 *J. Phys. D: Appl. Phys.* **55** 305202

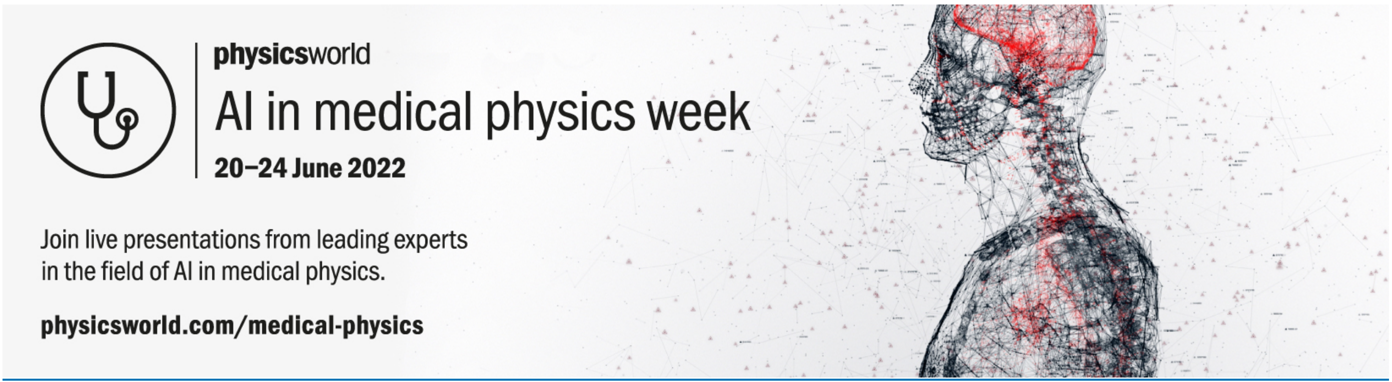

IOP Publishing Journal of Physics D: Applied Physics

J. Phys. D: Appl. Phys. **55** (2022) 305202 (11pp) https://doi.org/10.1088/1361-6463/ac6d24

Operation-mode recognition of surface microdischarge based on visible image and deep learning

Chen Lu[1], **Tao Peng**[2] **and Zilan Xiong**[1,*]

[1] State Key Laboratory of Advanced Electromagnetic Engineering and Technology, Huazhong University of Science and Technology, Wuhan, Hubei 430074, People's Republic of China
[2] Wuhan National High Magnetic Field Center, Huazhong University of Science and Technology, Wuhan, Hubei 430074, People's Republic of China

E-mail: zilanxiong@hust.edu.cn

Received 18 December 2021, revised 21 April 2022
Accepted for publication 5 May 2022
Published 18 May 2022

Abstract

Discharging images contain useful information regarding the operation mode of surface microdischarge (SMD). To solve the shortcomings of low efficiency, high cost, and long operation time of existing SMD operation-mode recognition methods, a convolutional neural network (CNN) based on deep learning is introduced herein. The visible image library of SMD at different applied voltages, dielectric sheets with different dielectric constants, and dielectric sheets with different thicknesses and exposure times are constructed using a digital camera. The typical structure of a CNN is discussed, and the hyperparameters, including the number of network layers, convolution kernel size, number of neurons in the fully connected layer, and activation function type that affect the recognition accuracy of the CNN are investigated. The optimal structure of the CNN for the SMD operation-mode recognition is obtained via training. The recognition accuracy of the CNN is compared with those of three traditional machine learning methods: support vector machine (SVM), decision tree (DT), and random forest (RF). Test results show that the recognition accuracy based on the CNN is 99.745%, which is better than those of the SVM, DT, and RF. Finally, an SMD operation-mode online recognition method based on the CNN is proposed.

Keywords: surface microdischarge, plasma diagnostic, convolutional neural network, visible image, operation-mode recognition

(Some figures may appear in colour only in the online journal)

1. Introduction

Surface microdischarge (SMD) has received significant attention because of its broad application prospects in food preservation [1, 2], agriculture [3, 4], material processing [5, 6], and biomedicine [7, 8]. SMD is a simple process that allows direct discharge in air without the use of a specific background gas; furthermore, it offers the advantages of low cost, high flexibility, and abundant chemical reactions [9–11]. Based on the dominant gas-phase products, the operation modes of SMD can be categorized into ozone, transition, and NO_x modes [12–16]. When O_3 is the main gas-phase production, SMD occurs in the ozone mode; when O_3 and NO_x are simultaneously detected in the main gas-phase production, SMD occurs in the transition mode; when NO_x is the main gas-phase production, SMD occurs in the NO_x mode.

Realizing fast, low-cost, reliable, and online operation-mode recognition is key in the practical application of SMD. The existing operation-mode recognition methods are

---

[*] Author to whom any correspondence should be addressed.

primarily completed using equipment such as a spectrometer, ozone detectors, and nitrogen oxide detectors. These methods involve offline detection as well as a specific detection environment or design relevant to detection devices; moreover, they are associated with disadvantages of long detection time, high detection cost, and complicated operation. For example, using Fourier transform infrared (FTIR) spectroscopy is a common way to detect operation modes of SMD in laboratory, the instrument is expensive and the measurement system usually requires additional absorption cell with IR windows. As for an O_3 or NO_x detector, it also needs to be connected to the whole system, and usually takes seconds or tens of seconds to obtain one stable result, the responding time and accuracy of which depends on the device cost. As the discharge, diagnostics, and application of SMD cannot be realized simultaneously using these methods, their industrial promotion and application are limited.

Various signals are generated by non-equilibrium plasmas (NEPs) during discharges, including electrical, acoustic, thermal, and optical signals [17–19]. Among them, diagnostic technology based on optical signals is important for analyzing the characteristics of NEPs [20, 21]. The optical signals released by NEPs includes ultraviolet, visible, and near-infrared signals [22]. Owing to the continuous development of digital image processing technology, studies regarding the visible image of NEPs has increased, and the scope of its application has become increasingly extensive [23, 24]. It has been reported that the visible image of NEPs can be used to categorize the discharge stage, classify the discharge mode, predict the discharge power, and quantify the discharge product [25–28]. The visible image of NEPs contains abundant discharge information, which can effectively reflect the discharge evolution. Furthermore, the diagnostic technology based on the visible image is a non-invasive diagnostic method and offers the advantages of low cost, simple operation, and high detection speed.

In recent years, owing to the rapid increase of artificial intelligence (AI), AI algorithms have been applied increasingly to the field of NEPs [29, 30]. Krüger *et al* applied the energy distribution of impinging projectile particles as the input of a multilayer perceptron network to accurately predict the energy and angular distributions of reflected and sputtered particles during thin-film deposition [31]. The effects of hyperparameters such as the number of hidden layers, number of neurons, and activation function type on the prediction accuracy were investigated. Ye *et al* used a digital camera to obtain visible images of corona discharge at different states and then extracted the color, brightness, and shape information of the discharging images to be used as the input of four different machine-learning algorithms, i.e. the support vector machine (SVM) [32], K-nearest neighbor [33], single layer perceptron [34], and decision tree (DT) [35], to predict the discharge voltage of corona discharge corresponding to different states [36]. Witman *et al* performed deep reinforcement learning to achieve real-time temperature control of atmospheric pressure plasma jets (APPJs) under different reaction conditions to solve the complex control problems of APPJs in practical applications [37]. AI exhibits the characteristics of simplicity, reliability, fast operation, and good application effects; hence, it has been successfully applied in the modeling, diagnostics, and control of NEPs.

To address the disadvantages of the existing operation-mode recognition method of SMD, an AI algorithm is introduced herein. FTIR was used to identify the gas-phase products of SMD under different discharge conditions and hence the corresponding operation mode. A digital camera was used to capture the visible image of the SMD in the corresponding operation mode. An SMD operation-mode online recognition method based on a convolutional neural network (CNN) is proposed herein. The number of network layers, convolution kernel size, number of neurons in the fully connected layer, and activation function type were investigated to obtain the optimal structure of the CNN for the operation-mode recognition of SMD. The recognition accuracy of the optimized CNN was discovered to be the highest compared with those of the other three traditional machine-learning methods.

2. Experimental setup and measurements

2.1. Experimental setup

Figure 1(a) shows the structure of the SMD device used in this study. A typical SMD device with a sandwich structure was placed on top of a cylindrical acrylic chamber with a diameter of 38 mm and a height of 45 mm. Two ZnSe windows were mounted on the wall of the chamber to transmit an IR beam to analyze the composition of the gas-phase products. A high-voltage and high-frequency AC power supply (Corona Lab, CTP-2000K) was used as the power source. More details regarding the experimental setup are available in the literature [38]. The flowchart of the method proposed in this study is shown in figure 1(b). Firstly, an image library was constructed, 70% of the images were used for training and 30% of the images were used for testing. Then, the construction of the CNN was established, and the hyperparameters of the CNN model were optimized, including the number of network layers, convolution kernel size, activation function type, and number of neurons in the fully connected layer. Finally, the performance of the CNN model was evaluated.

To construct a discharge image library of SMD, two types of dielectric sheets with three different thicknesses were used in this study, as shown in table 1.

2.2. Measurements and methods

For all experiments, the frequency of the AC power supply (CTP-2000K, Corona Lab) was fixed at 8 kHz. A voltage probe (Tektronix P6015A) and an oscilloscope (Tektronix MDO3034) were used to monitor the applied AC voltage amplitude. A current probe (Pearson 6585) was used to measure the circuit current. To determine the power consumed by the SMD device, using the Lissajous method, a 10 nf capacitor was connected in series between the mesh and ground, and the voltage across the capacitor was measured using a differential probe (Tektronix P5200A).

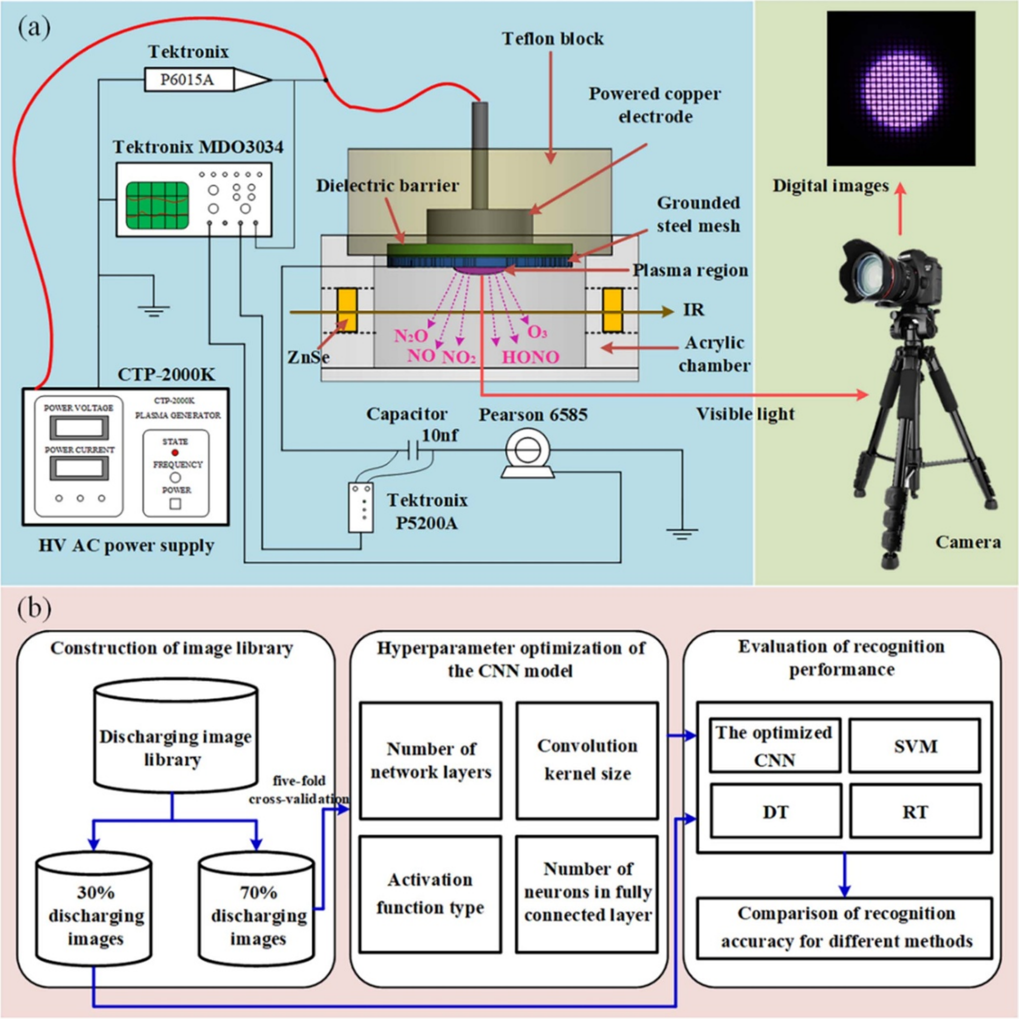

Figure 1. (a) Illustration of SMD device and experiment setup. (b) The flowchart of the method proposed in this study.

Table 1. Two types of dielectric sheets used in this study.

Dielectric sheet	Dielectric constant	Thickness (mm)
Al_2O_3	9.3	0.5, 1, 2
ZrO_2	12.5	0.5, 1, 2

The chemical composition of the gas produced by the SMD device was determined *in situ* realized using FTIR (Bruker, VERTEX 70). The wavenumber resolution of the FTIR measurements was set to 4 cm^{-1}, and 16 scans were averaged to create each spectrum. The time resolution of each spectrum was 15 s. The primary gas-phase products generated by the SMD device included N_2O, NO, NO_2, HONO, and O_3.

As shown in figure 1, a digital camera (NIKON D750) was used to obtain discharge images of the SMD under different discharging conditions against a dark background. The main camera parameters were set as follows: aperture $f = 5.6$ and ISO = 2000. Meanwhile, default values were assigned to the remaining parameters. For the same discharging condition, the discharging images of SMD under different exposure times were recorded, including 30, 25, 20, 15, 10, 8, 6, 4, 2, 1, 1/2, 1/4, 1/6, 1/8, 1/10, 1/15, and 1/20 s.

2.3. *CNN*

In recent years, the rapid development of computer technology has increased the application of deep learning in many fields [39, 40]. As a form of deep learning, CNNs have been widely used in natural language processing [41], speech recognition [42], face recognition [43], object detection [44], and medical diagnosis [45]. The CNN is based on the basic principles of a biological visual neural network [46]. A CNN is a feedforward neural network that involves few network parameters, low computational complexity, and high generalization ability.

A typical CNN is primarily composed of an input layer, a convolutional layer, a pooling layer, a fully connected layer, and an output layer [47], as shown in figure 2. The input layer is used to input the original data into the network. The convolutional layer, which affords local connections and weight sharing, is used to extract the feature map from the input data. The pooling layer uses the output of the convolutional layer as

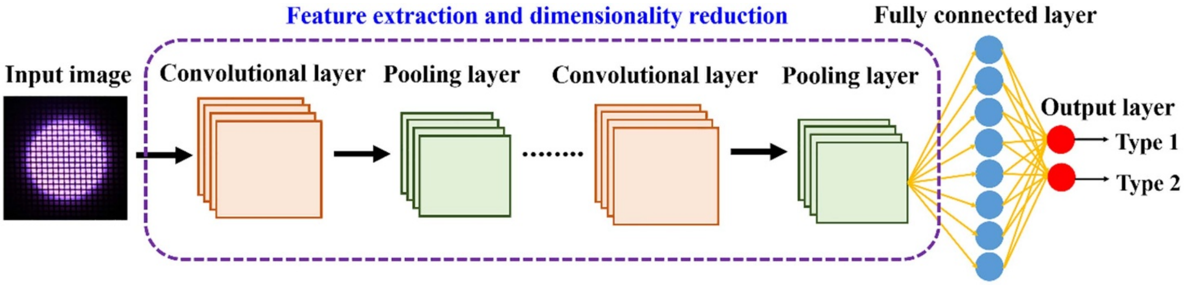

Figure 2. Typical structure of CNN.

input. It down samples the feature map extracted by the convolutional layer to reduce the dimension of the feature map, avoid the occurrence of overfitting, and obtain the main features of the input data. The pooling layer is primarily implemented via max pooling. The convolutional and pooling layers are alternately connected to realize automatic feature extraction and input data compression, while reducing the training time of the network. The fully connected layer is located behind the convolutional and pooling layers. It is similar to the traditional neural network structure and is used to integrate the features extracted by the convolutional and pooling layers. The output layer is the final result of the network output.

The recognition performance of a CNN is associated with its hyperparameters, including the number of network layers, convolution kernel size, number of neurons in the fully connected layer and activation function type. We tested and compared the recognition accuracy for each hyperparameter: (a) for the number of network layers, the testing variables include 5, 7, 9, 11 and 13 layers; (b) for convolution kernel size, 1×1, 2×2, 3×3 and 4×4 were tested; (c) for number of neurons in the fully connected layer, the results of 64, 128, 256, 512 and 1028 neurons were compared; (d) for the activation function type, the sigmoid, hyperbolic tangent function (tanh), rectified linear unit (ReLU), and self-gated activation function (swish) were tested. The equations of these four function type are shown below:

$$\mathrm{sigmoid}\,(x) = \frac{1}{1 + \mathrm{e}^{-x}} \tag{1}$$

$$\tan\,(x) = \frac{\mathrm{e}^{x} - \mathrm{e}^{-x}}{\mathrm{e}^{x} + \mathrm{e}^{-x}} \tag{2}$$

$$\mathrm{relu}\,(x) = \max\,(0, x) \tag{3}$$

$$\mathrm{swish}\,(x) = x \times \mathrm{sigmoid}\,(x)\,. \tag{4}$$

More details of how these hyperparameter affect the performance will be presented and discussed in section 3.4.

2.4. Construction of image library

We acquired visible images of SMD under different discharging conditions, including dielectric sheets with different dielectric constants, dielectric sheets with different thicknesses, applied voltages, and different exposure times. We obtained 7852 discharge images of SMD under different conditions to form the image library. Among them, 3926 discharging images corresponded to the ozone and non-ozone modes. All the discharging images were randomly categorized into training, validation, and test sets. In fact, 70% of the discharging images was used for training and validating the CNN, and 30% of the discharging images was used for testing the trained CNN. We performed five-fold cross-validation, i.e. 70% of the discharging images was randomly segregated into five groups, four of which were used as the training set, and the remaining was used for the validation set. The hyperparameters of the CNN were learned and optimized using the backpropagation algorithm and applying the Adam update scan during training. The final performance of the CNN was evaluated using the test set.

To establish and train the CNN, Tensorflow framework 1.12.0 and Keras API 2.2.4 were used. To accelerate the training process, CUDA 10.2 and two NVIDIA GPUs (GeForce RTX 2080) were employed. The time required for the training process of the CNN was within 1 h, and for the testing process, the time was about 2 s.

3. Results and discussion

3.1. Typical FTIR spectrum of SMD

Figure 3 shows the typical FTIR spectrum of the SMD device comprising a 1 mm Al_2O_3 dielectric sheet. When the applied voltage $V_{\text{p-p}}$ was 6 kV, the main gas-phase product was O_3 (1055 cm^{-1}); therefore, we defined the SMD device operating in the ozone mode. When the applied voltage $V_{\text{p-p}}$ was 12 kV, the main gas-phase products were nitrogen oxides, including NO (1900 cm^{-1}), NO_2 (1630 cm^{-1}), and HONO (1255 cm^{-1}); therefore, we defined the operation mode as ‘non-ozone’ in our study.

3.2. Classification of operation modes for SMD based on FTIR

Figure 4 shows the operation modes for the SMD under different conditions detected via FTIR. When the thicknesses of the Al_2O_3 dielectric sheet were 0.5, 1, and 2 mm, the transfer voltages from the ozone mode to the non-ozone mode of the SMD were 5.5, 7.5, and 11.5 kV, respectively. Meanwhile,

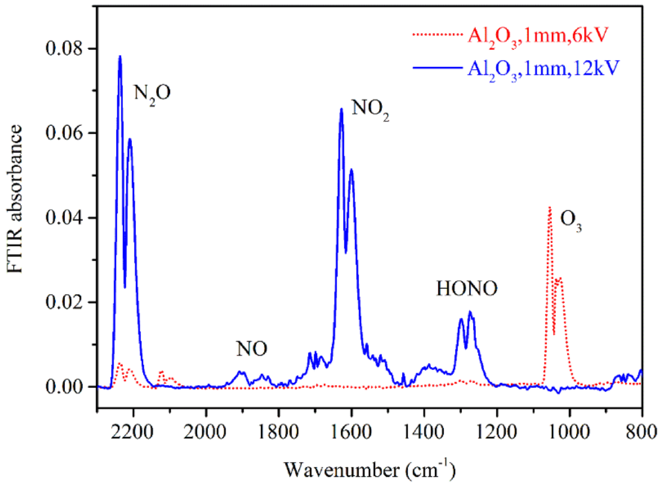

Figure 3. Typical FTIR spectrum of SMD device comprising 1 mm Al_2O_3 dielectric sheet under different applied voltages.

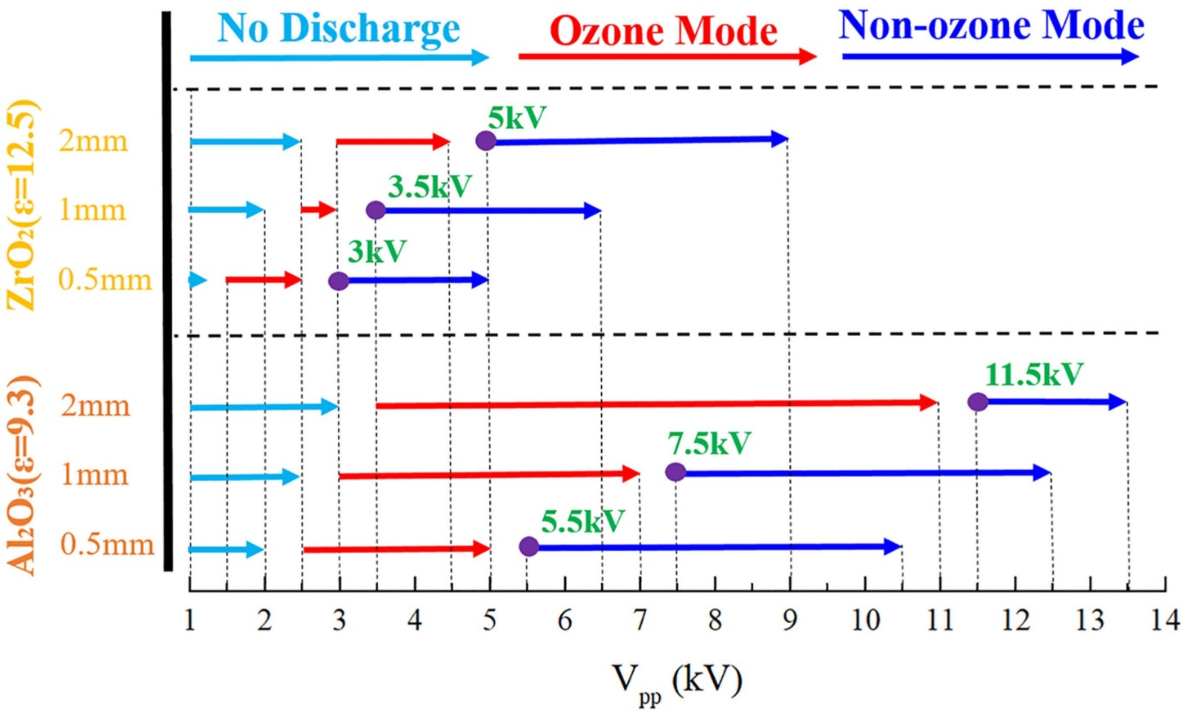

Figure 4. Classification of operation modes for SMD via FTIR.

when the thickness of the ZrO_2 dielectric sheet was 0.5, 1, and 2 mm, the transfer voltage from the ozone mode to the non-ozone mode of the SMD was 3, 3.5, and 5 kV, respectively. For dielectric sheets of the same dielectric constant, the transfer voltage for different SMD operation modes increased with the thickness of the dielectric sheet. For dielectric sheets of the same thickness, the transfer voltage for different SMD operation modes decreased with the increase in the dielectric constant. Furthermore, it was discovered that the SMD operation modes could not be distinguished via only the discharge voltage.

3.3. Typical discharging color images of SMD

Figure 5 shows the discharging color images of the SMD device corresponding to Al_2O_3 and ZrO_2 dielectric sheets with thicknesses of 0.5, 1, and 2 mm when the applied voltage $V_{p\text{-}p}$ was 4.5 kV. Under a constant applied voltage $V_{p\text{-}p}$, for dielectric sheets with the same dielectric constant, when the thickness of the dielectric sheet was smaller, the discharge power consumption of the SMD device and the discharging area of the discharging images were greater; additionally, the discharge intensity and discharge brightness of the discharging

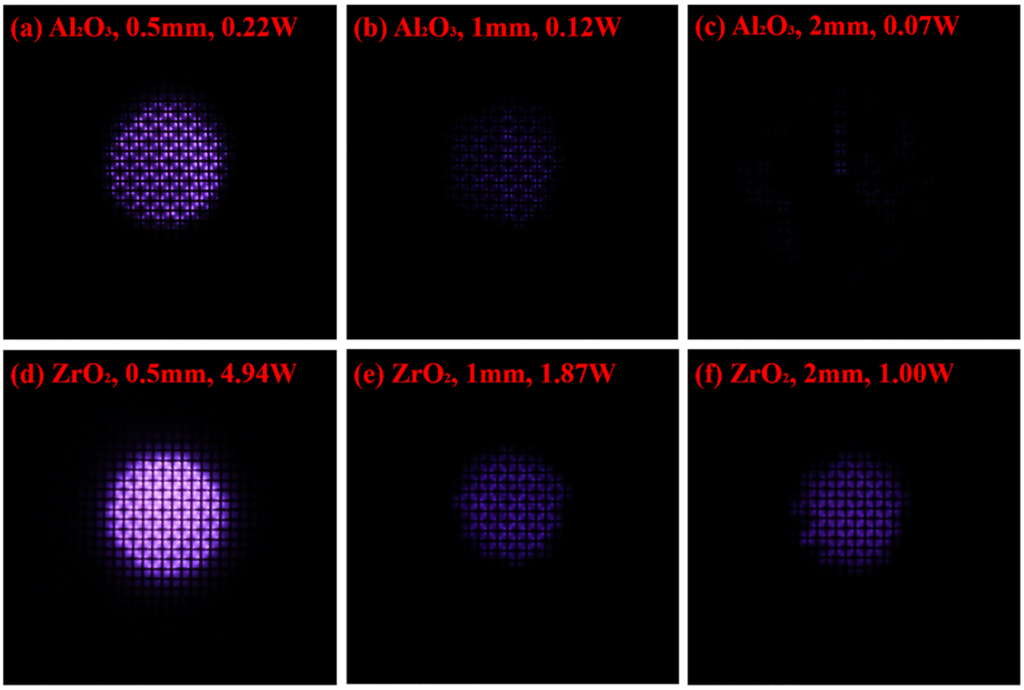

Figure 5. Discharging images of SMD device corresponding to Al_2O_3 and ZrO_2 dielectric sheets with thicknesses of 0.5, 1, and 2 mm. Applied voltage $V_{\text{p-p}}$ was 4.5 kV; exposure time of the camera was 1 s.

images were higher. For dielectric sheets of the same thickness, when the dielectric constant of the dielectric sheet was smaller, the discharge power consumption of the SMD device and the discharging area of the discharging images were smaller, additionally, the discharge intensity and discharge brightness of the discharging images were lower.

3.4. Analysis of hyperparameters

3.4.1. Selection of the number of epochs for the training of the model. Figure 6 shows the training and validation loss of CNN. It can be seen that, the training and validation loss gradually decreases to be stable and the difference between the two final loss values is small. The number of epochs selected for the training of CNN is 100.

3.4.2. Effect of the number of network layers. Feature extraction and dimensionality reduction of input data are realized through the convolutional and pooling layers of the CNN. The number of convolutional and pooling layers reflects the number of network layers. The number of network layers, i.e. the depth of the network, is associated closely with the performance of the CNN. The greater the number of network layers, the better is the nonlinear expression ability of the CNN, and the easier it is to capture the complex transformations between the input and output. However, as the number of network layers increases, the risk of overfitting may increase. Furthermore, excessive network layers may limit the learning ability of the shallow network in the CNN and reduce the learning efficiency of the network.

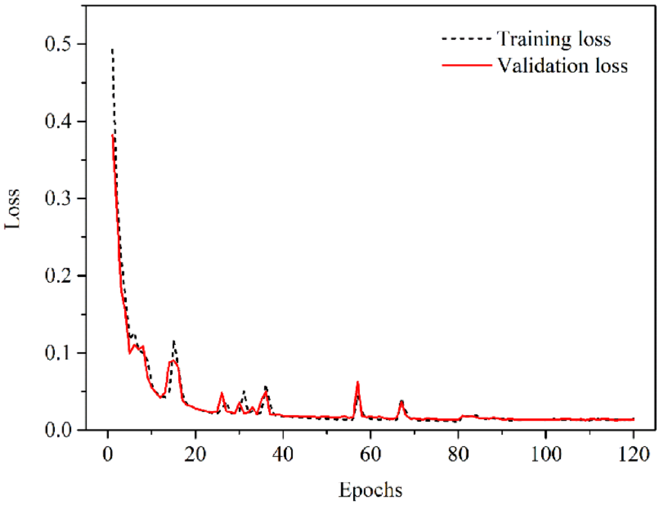

Figure 6. Training and validation loss of CNN.

Figure 7 shows the effect of the number of network layers of the CNN on the accuracy of the operation-mode recognition of SMD. The five types of CNNs with different numbers of network layers contained the same numbers of input and output layers, and the convolution kernel size, number of neurons in the fully connected layer, and activation function type were the same: 3 × 3, 512, and tanh, respectively. The first type of CNN contained one input layer, one convolutional layer, one pooling layer, one fully connected layer, and one output layer; therefore, the total number of network layers was five. Meanwhile, the second type of CNN contained one input layer, two convolutional layers, two pooling layers, one fully connected

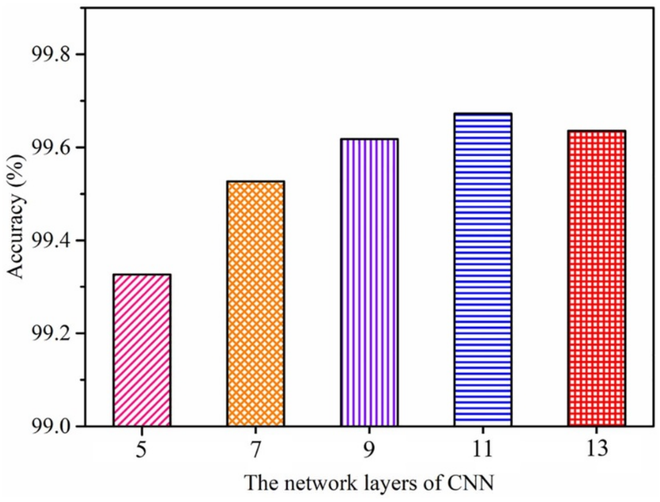

Figure 7. Comparison of recognition accuracy for CNNs with different numbers of network layers.

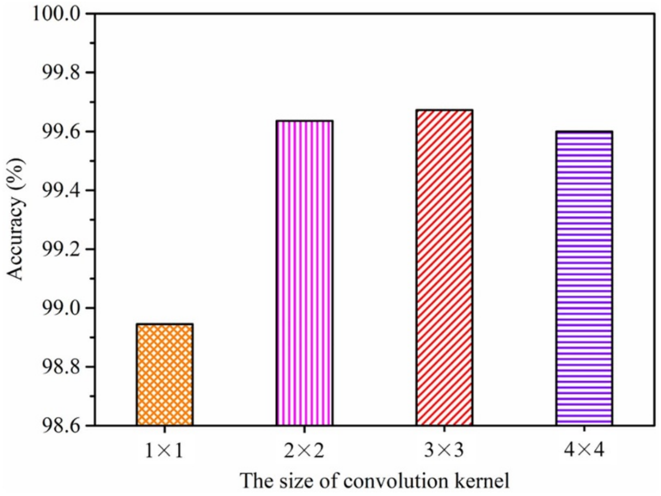

Figure 8. Comparison of recognition accuracy for CNNs with different convolution kernel sizes.

layer, and one output layer; therefore, the total number of network layers was seven. The third to fifth types of the CNN contained one input layer, five convolutional layers, five pooling layers, one fully connected layer, and one output layer; therefore, the total number of network layers was 13. The results show that the recognition accuracy of the SMD operation mode increased with the number of network layers initially, and that when the number of network layers was 11, the maximum training accuracy of 99.672% was achieved. However, as the number of network layers continued to increase, the recognition accuracy began to decrease. Therefore, the optimal number of network layers for the CNN was 11.

3.4.3. Effect of the convolution kernel size. The convolution kernel is vital to the convolutional layer in a CNN. The parameters of the convolution kernel are shared during feature extraction. This parameter-sharing method can effectively reduce the number of training parameters for a CNN. The amount of information that the convolutional layer extracts from the input and the amount of calculation for the network are associated with the convolution kernel size. The larger the convolution kernel size, the greater is the amount of information that can be extracted by the convolution layer, and the easier is the extraction of effective features from the input. Simultaneously, the number of calculations for the network is increased, resulting in increased network complexity. The smaller the convolution kernel size, the less is the amount of information extracted by the convolution layer, which may cause the loss of important information from the input features. However, the training cost of a network can be reduced.

As shown in figure 8, we analyzed the effect of the convolution kernel size of the CNN on the accuracy of the operation-mode recognition of SMD. The four types of CNN with different convolution kernel sizes contained the same numbers of input and output layers, and the number of network layers, number of neurons in the fully connected layer, and activation function type were the same: 11, 512, and tanh, respectively. The results indicate that when the size of the convolution kernel was 3 × 3, the recognition accuracy was the highest, i.e. 0.728%, 0.036%, and 0.073% higher than those obtained by convolution kernel sizes of 1 × 1, 2 × 2, and 4 × 4, respectively. It was discovered that the optimal size of the convolution kernel for the CNN was 3 × 3.

3.4.4. Effect of the number of neurons in fully connected layer. The number of neurons in the fully connected layer directly affects the performance of the CNN. If the number of neurons is extremely small, then the trained network cannot effectively capture the feature space of the input data; this may easily cause an underfitted network, thereby resulting in subpar network performance. If the number of neurons is extremely high, network training will be difficult, and the demand for training data may increase; in other words, more data are required to train the network, the network may be overfitted. Selecting an appropriate number of neurons in the fully connected layer is important when training the CNN.

Figure 9 shows the effect of the number of neurons in the fully connected layer of the CNN on the accuracy of the operation-mode recognition of SMD. The five types of CNN with different numbers of neurons in the fully connected layer contained the same numbers of input and output layers, and the number of network layers, convolution kernel size, and activation function type were the same: 11, 3 × 3, and tanh, respectively. The results indicate that when the number of neurons in the fully connected layer was 512, the recognition accuracy was the highest, i.e. 0.018%, 0.055%, 0.073%, and 0.036% higher than those afforded by 64, 128, 256, and 1024 neurons, respectively. The optimal number of neurons in the fully connected layer was 512.

3.4.5. Effect of the activation function type. The convolutional, pooling, and fully connected layers of the CNN implement the linear transformation of the input data, and the activation function is applied to map the linear output of the

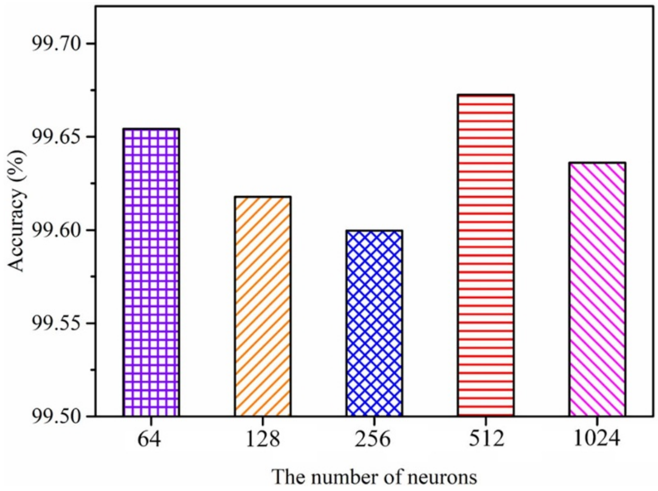

Figure 9. Comparison of recognition accuracy for CNNs with different numbers of neurons in fully connected layer.

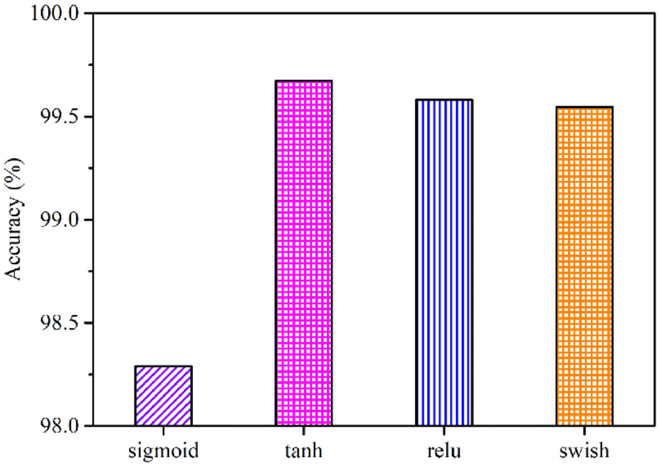

Figure 10. Comparison of recognition accuracy for CNNs with different activation functions.

network to the nonlinear space, thereby increasing the ability of the network in accomplishing complex tasks.

As shown in figure 10, the accuracies of the operation-mode recognition of SMD for different activation function types of the CNN are presented. The four types of CNNs with different activation functions contained the same number of input layer and output layer, and the number of network layers, the convolution kernel size, and number of neurons in the fully connected layer were the same: 11, 3 × 3, and 512, respectively. The results show that when the activation function type was tanh, the recognition accuracy was the highest, i.e. 1.383%, 0.091%, and 0.127% higher than those afforded by the sigmoid, ReLU, and swish functions, respectively. Therefore, the optimal activation function was the tanh function.

3.5. Comparison of different recognition methods

Based on the hyperparameters of the CNN, we determined the optimal structure of the CNN for the operation-mode recognition of SMD. The structure of the final selected CNN was as follows: the number of network layers was 11; convolution kernel size, 3 × 3; number of neurons in the fully connected layer, 512; activation function, tanh. Figure 11 shows the confusion matrix for different recognition methods. The degree of confusion among the CNN recognition results of ozone mode and non-ozone mode is: 5 of the 1182 samples of non-ozone mode are misidentified as ozone mode; 1 of the 1174 samples of ozone mode are misidentified as non-ozone mode, which is better than those of the SVM, DT, and random forest (RF).

As shown in figure 12, we used the optimized CNN to evaluate on the test set. Moreover, we compared the performance of the CNN with those of the SVM, DT, and RF [48]. The results show that the testing accuracy for the operation-mode recognition of the SMD based on the proposed CNN was 99.745%, which was 8.276%, 2.461%, and 0.551% higher than those of the SVM, DT, and RF, respectively. Table 2 shows the accuracy, precision, recall and F1-score of different recognition methods. It can be seen that, the accuracy, precision, recall and F1-score of the CNN are the highest compared to the other methods.

In conventional machine-learning algorithms such as the SVM, DT, and RF, data analysis is typically performed on the samples prior to training. The features input into the model must be selected manually. It is well known that the recognition accuracy of a model associated significantly with the selected features. If the training samples are directly input into the model or the manually selected features are not highly correlated model training will be difficult, which will result in a lower recognition accuracy of the model. However, the original images can be directly used as input to the CNN. Feature extraction and operation-mode recognition can be automatically completed by the CNN to promptly implement the mapping relationship between the input and output, as well as avoid complicated and time-consuming feature engineering. Compared with conventional machine-learning algorithms, CNN involves a simpler training process, and its recognition accuracy is higher. Other deep learning algorithms may also have similar recognition accuracy up to 99.745% as CNN with appropriate parameter adjustment, such as long short term

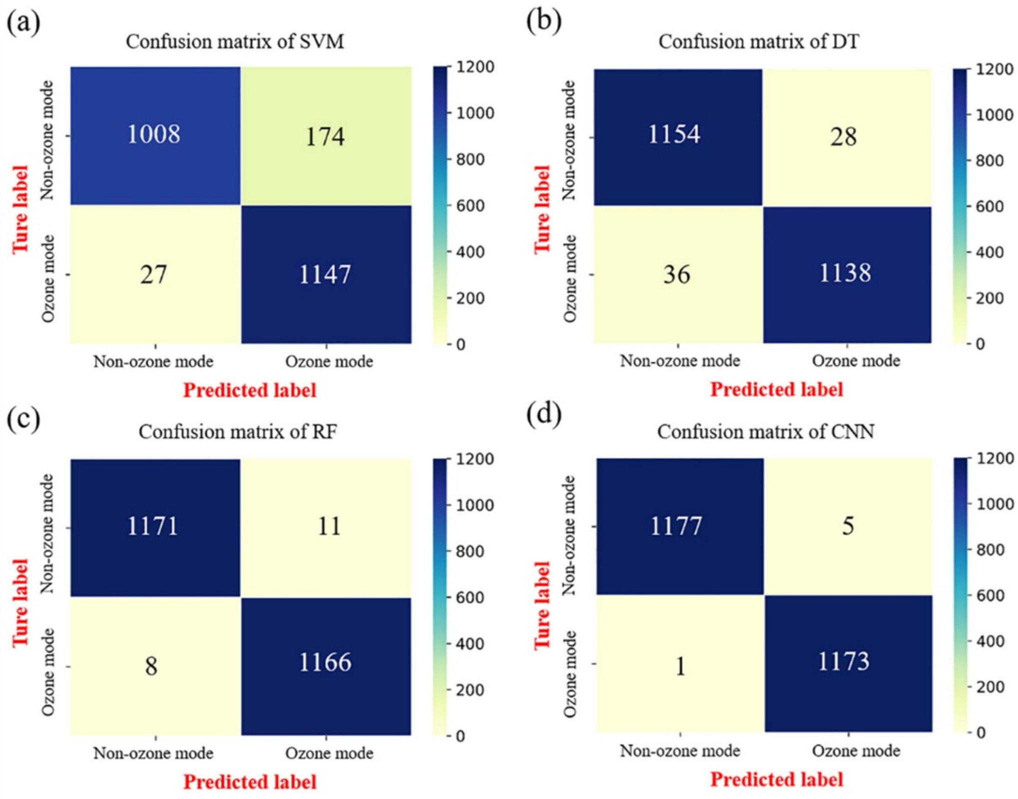

Figure 11. Confusion matrix for (a) SVM, (b) DT, (c) RF, (d) CNN.

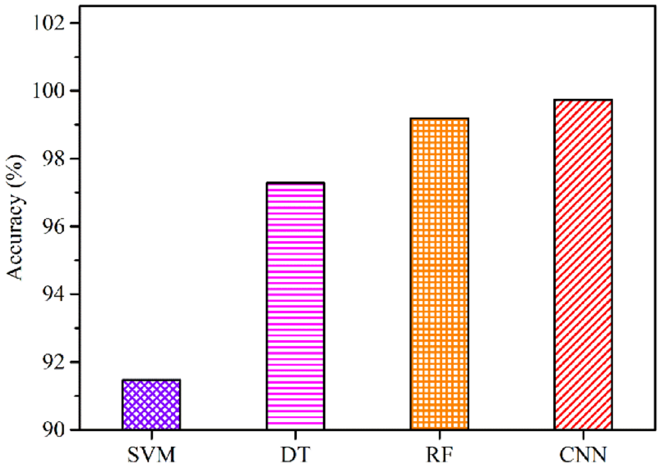

Figure 12. Comparison of recognition accuracy for different SMD operation-mode recognition methods.

Table 2. The accuracy, precision, recall and F1-score of different recognition methods.

Methods	Accuracy	Precision	Recall	F1-score
SVM	0.914 69	0.868 28	0.977 00	0.919 44
DT	0.972 84	0.975 99	0.969 34	0.972 65
RF	0.991 94	0.990 65	0.993 19	0.991 92
CNN	0.997 45	0.995 76	0.999 15	0.997 45

memory [49], ResNet [50], MLeNet [51], faster region-based CNN [52], and these algorithm constructions and accuracy comparison will be conducted in our following work.

4. Concluding remarks

In this study, the deep learning methodology was applied to SMD operation-mode recognition. SMD images contain abundant information regarding its operation mode, which is an effective basis for operation-mode recognition. In fact, SMD images can be directly input into the CNN, thereby avoiding the complicated process of feature extraction and selection. The number of network layers, convolution kernel size, number of neurons in the fully connected layer, and activation function type affect the recognition accuracy of the CNN. For SMD operation-mode recognition, the optimal structure of the CNN was as follows: the number of network layers was 11; convolution kernel size, 3 × 3; number of neurons in the fully connected layer, 512; activation function, tanh. Compared with other conventional machine-learning methods, i.e. the SVM, DT, and RF, the CNN afforded higher recognition accuracy. Hence, the CNN is envisioned as a promising method for the online recognition of the SMD operation mode with low cost, simple operation, high detection speed and accuracy.

Data availability statement

The data that support the findings of this study are available upon reasonable request from the authors.

Acknowledgments

The authors are grateful for financial support from the National Natural Science Foundation of China (Nos. 51907076 and 52177145).

ORCID iDs

Tao Peng https://orcid.org/0000-0002-8287-3723
Zilan Xiong https://orcid.org/0000-0003-1095-3959

References

[1] Zhou R, Zhou R, Mai-Prochnow A, Zhang X, Xian Y, Cullen P J and Ostrikov K 2020 *J. Phys. D: Appl. Phys.* **53** 174003
[2] Song Y, Liu D, Lu Q, Xia Y, Zhou R, Yang D, Ji L and Wang W 2015 *IEEE Trans. Plasma Sci.* **43** 821–7
[3] Cui D, Yin Y, Wang Z, Ding H, Ma R and Jiao Z 2019 *Front. Plant Sci.* **10** 1322
[4] Song J-S, Lee M J, Ra J E, Lee K S, Eom S, Ham H M, Kim H Y, Kim S B and Lim J 2020 *J. Phys. D: Appl. Phys.* **53** 314002
[5] Lu C, Dai J, Dong N, Zhu Y and Xiong Z 2020 *Plasma Process. Polym.* **17** e2000100
[6] Knoll A J, Luan P, Pranda A, Bruce R L and Oehrlein G S 2018 *Plasma Process. Polym.* **15** e1700217
[7] Xiong Z, Huang R, Zhu Y, Luo K, Li M, Zou Z and Han R 2021 *Plasma Process. Polym.* **18** e2000204
[8] Wang X, Wang W, Liu Z, Wang Z, Guo L, Wang X, Rong M and Liu D 2020 *Plasma Sources Sci. Technol.* **29** 095013
[9] Shimizu T, Sakiyama Y, Zimmermann J L and Morfill G E 2011 *New J. Phys.* **13** 023026
[10] Li D, Liu D, He T, Li Q, Wang X and Kong M G 2015 *Phys. Plasmas* **22** 123501
[11] Liu D, Liu Z, Chen C, Yang A, Li D, Rong M Z, Chen H and Kong M G 2016 *Sci. Rep.* **6** 23737
[12] Pavlovich M J, Clark D S and Graves D B 2014 *Plasma Sources Sci. Technol.* **23** 065036
[13] Shimizu T, Sakiyama Y, Graves D B, Zimmermann J L and Morfill G E 2012 *New J. Phys.* **14** 103028
[14] Sakiyama Y, Graves D B, Chang H-W, Shimizu T and Morfill G E 2012 *J. Phys. D: Appl. Phys.* **45** 425201
[15] Maisch T, Shimizu T, Isbary G, Heinlin J, Karrer S, Klämpfl T G, Li Y-F, Morfill G E and Zimmermann J L 2012 *Appl. Environ. Microbiol.* **78** 4242
[16] Zimmermann J L, Dumler K, Shimizu T, Morfill G E, Wolf A, Boxhammer V, Schlegel J, Gansbacher B and Anton M 2011 *J. Phys. D: Appl. Phys.* **44** 505201
[17] Guo L, Li L, Dong F and Jiang W 2017 *Sci. Rep.* **7** 9475
[18] Aleksandrov N L, Kindysheva S V, Nudnova M M and Starikovskiy A Y 2010 *J. Phys. D: Appl. Phys.* **43** 255201
[19] Gherardi M, Puač N, Marić D, Stancampiano A, Malović G, Colombo V and Petrović Z L 2015 *Plasma Sources Sci. Technol.* **24** 064004
[20] Bruggeman P J, Sadeghi N, Schram D C and Linss V 2014 *Plasma Sources Sci. Technol.* **23** 023001
[21] Voráč J, Synek P, Procházka V and Hoder T 2017 *J. Phys. D: Appl. Phys.* **50** 294002
[22] Yuan Z, Ye Q, Wang Y and Guo Z 2021 *IEEE Trans. Instrum. Meas.* **70** 5004511
[23] Ye Q, Yu D, Yang F and Tan D 2013 *IEEE Trans. Plasma Sci.* **41** 540–4
[24] Li X, Ye Q, Gu W, Chen R, Wang Z, Rao Z, Hu Y and Jang Z 2016 *IEEE Trans. Dielectr. Electr. Insul.* **23** 165–73
[25] Wu Y, Ye Q, Li X and Tan D 2012 *IEEE Trans. Plasma Sci.* **40** 1371–9
[26] Guo Z, Ye Q, Li F and Wang Y 2019 *IEEE Trans. Dielectr. Electr. Insul.* **26** 1448–55
[27] Zou Z, Han R, Lu C and Xiong Z 2021 *Plasma Process. Polym.* **18** e2000139
[28] Prasad D S and Reddy B S 2017 *IEEE Trans. Dielectr. Electr. Insul.* **24** 75–82
[29] Wang C Y and Hsu C C 2019 *Plasma Sources Sci. Technol.* **28** 105013
[30] Mesbah A and Graves D B 2019 *J. Phys. D: Appl. Phys.* **52** 30LT02
[31] Krüger F, Gergs T and Trieschmann J 2019 *Plasma Sources Sci. Technol.* **28** 035002
[32] Cortes C and Vapnik V 1995 *Mach. Learn.* **20** 273–97
[33] Hastie T and Tibshirani R 1996 *IEEE Trans. Pattern Anal. Mach. Intell.* **18** 607–16
[34] Raudys S 1998 *Neural. Netw.* **11** 283–96
[35] Breslow L A and Aha D W 1997 *Knowl. Eng. Rev.* **12** 1–40
[36] Ye Q, Ye P, Guo Z, Dong X and Wang M 2020 *IEEE Trans. Plasma Sci.* **48** 31–35
[37] Witman M, Gidon D, Graves D B, Smit B and Mesbah A 2019 *Plasma Sources Sci. Technol.* **28** 095019
[38] Lu C, Chen X, Wang Y, Zhu Y, Zou Z and Xiong Z 2021 *Plasma Process. Polym.* **19** e2100107
[39] Schmidhuber J 2015 *Neural Netw.* **61** 85–117
[40] LeCun Y, Bengio Y and Hinton G 2015 *Nature* **521** 436–44
[41] Giménez M, Palanca J and Botti V 2020 *Neurocomputing* **378** 315–23

[42] Abdel-Hamid O, Mohamed A, Jiang H, Deng L, Penn G and Yu D 2014 *IEEE Trans. Audio Speech Lang. Process.* **22** 1533–45
[43] Yin X and Liu X 2018 *IEEE Trans. Image Process.* **27** 964–75
[44] Ševo I and Avramović A 2016 *IEEE Geosci. Remote Sens. Lett.* **13** 740–4
[45] Yang Z, Huang Y, Jiang Y, Sun Y, Zhang Y and Luo P 2018 *Sci. Rep.* **8** 6329
[46] Uchida K, Tanaka M and Okutomi M 2018 *Neural Netw.* **105** 197–205
[47] Feng J, Li F, Lu S, Liu J and Ma D 2017 *IEEE Trans. Instrum. Meas.* **66** 1883–92
[48] Breiman L 2001 *Mach. Learn.* **45** 5–32
[49] Kamat P V, Sugandhi R and Kumar S 2021 *PeerJ. Comput. Sci.* **7** e795
[50] Kadam V, Kumar S, Bongale A, Wazarkar S, Kamat P and Patil S 2021 *Appl. Syst. Innov.* **4** 34
[51] Lin S, Cai L, Lin X and Ji R 2016 *Neurocomputing* **218** 197–202
[52] Huang H, Zhou H, Yang X, Zhang L, Qi L and Zang A-Y 2019 *Neurocomputing* **337** 372–84